De, Swarnalok; Nguyen, Hoang M.; Zou, Fangxin; Basarir, Fevzihan; Mousavi, Maryam; Mäkinen, Kristiina; Kostiainen, Mauri A.; Vapaavuori, Jaana

Bio-Templated Silver Nanopatterns for Photothermal and Antifogging Coatings

Published in:
Advanced Materials Interfaces

DOI:
10.1002/admi.202300828

Published: 23/02/2024

Document Version
Publisher's PDF, also known as Version of record

ADVANCED MATERIALS INTERFACES
Open Access
www.advmatinterfaces.de

Bio-Templated Silver Nanopatterns for Photothermal and Antifogging Coatings

Swarnalok De, Hoang M. Nguyen, Fangxin Zou, Fevzihan Basarir, Maryam Mousavi, Kristiina Mäkinen, Mauri A. Kostiainen, and Jaana Vapaavuori**

Transparent photothermal coatings based on plasmonic noble metals often face a trade-off between achieved temperatures and transmittances. This challenge arises from the fact that plasmonic nanoparticles (NPs), which rely on their size and structures, selectively absorb light of various wavelengths and convert it into heat. In the cases of randomly arranged plasmonic NPs, absorbances are predominantly in the visible range, leading to lowered transmittances. In this work, the self-assembly behavior of a biotemplate containing flexible potato virus A (PVA) is used to produce network-like surface patterns with controllable intermittent vacancies. These templates effectively anchor silver nanoparticles (AgNPs), forming dense arrays of plasmonic hotspots interspersed with vacant regions. With this approach, a temperature increase of 21 °C above ambient temperature under 1-sun radiation is achieved while maintaining a visible light transmittance as high as 78% measured at 550 nm wavelength. The PVA biotemplated AgNPs show excellent potential as antifogging coating, exhibiting 2–3 times faster defogging rates compared to uncoated samples in both indoor and outdoor conditions. Overall, a platform is presented for biotemplating metal NPs, the development of long-range surface patterns with controlled vacancies, and the demonstration of transparent photothermal activity with an antifogging application.

1. Introduction

At the nanoscale, nanoparticles (NPs) exhibit unique behavior compared to their bulk state in terms of chemical, electrical, thermal, and biological characteristics.[1] Moreover, the deliberate arrangement of NPs in an organized manner leads to the emergence of metamaterials possessing distinct properties arising from both material composition and structural factors. Such controlling of NP patterns is a crucial success factor in optics and plasmonics.[2] An intriguing application of this is the development of transparent photothermal coatings.[3] The creation of well-organized and defect-free NP ordering has attracted massive research attention, with NP self-assembly standing out as a powerful bottom-up manufacturing technique.

Plant virus nanoparticles (VNPs) are promising candidates for constructing self-assembled nanostructures.[4,5] They are derived from biological sources, facile to be prepared renewably in large quantities, monodisperse in size, and completely non-toxic to the animal kingdom.[6] The VNPs possess a protective protein shell, also known as the "capsid".[7] The capsid consists of thousands of chemically reactive amino acid side chains that enable diverse surface modification probabilities.[8–10] Consequently, VNPs serve as excellent templates for the assembly of foreign materials. Prominent examples include cowpea mosaic virus (CPMV) and tobacco mosaic virus (TMV), both of which have been extensively utilized as biotemplates for the assembly of metallic NPs. Electroless deposition of Co, Ni, Fe, and Pt was performed on CPMV, while Pt, Pd, and Au NPs were deposited on TMV via electrostatic interaction.[11–13] These studies demonstrate the vast potential of VNPs in various applications, ranging from nanoelectronics to nanocatalyst synthesis.

S. De, H. M. Nguyen, F. Zou, F. Basarir, M. Mousavi, J. Vapaavuori
Department of Chemistry and Materials Science
Aalto University
Aalto 00076, Finland
E-mail: jaana.vapaavuori@aalto.fi

The ORCID identification number(s) for the author(s) of this article can be found under https://doi.org/10.1002/admi.202300828

DOI: 10.1002/admi.202300828

K. Mäkinen
Department of Agricultural Sciences
University of Helsinki
Helsinki 00790, Finland

M. A. Kostiainen
Department of Bioproducts and Biosystems
Aalto University
Aalto 00076, Finland
E-mail: mauri.kostiainen@aalto.fi

The process of nonradiative light-to-heat conversion can be achieved through light absorption.[14,15] The photothermal conversion by plasmonic NPs like Au and Ag occurs when they absorb light of a certain wavelength that induces localized surface plasmon resonance (LSPR) causing the electrons to jump to an excited state. In plasmonic hotspots where NPs are closely packed, the absorption of light leads to the generation of hot electrons. The heat is then transferred to the metal lattice through electron–phonon coupling.[16] Depending on the shape and size of the nanoparticle, the LSPR, as well as the heating wavelength can vary from UV–vis to NIR range.[16] In recent years, various plasmonic nanomaterials have garnered wide acceptance in the development of photothermal surfaces.[3,17,18] Although both AuNPs and AgNPs, owing to their strong plasmonic nature, have dominated the field of photothermal applications, particularly in the biomedical sector for photothermal therapeutics,[19–24] existing literatures show a bias toward the use of AuNPs in the development of transparent photothermal surfaces. However, a recent study comparing AuNPs and AgNPs for photothermal heating demonstrated that AgNPs below 20 nm in size can achieve higher temperature elevation than AuNPs.[25] Nevertheless, incorporating plasmonic NPs into the development of transparent photothermal surfaces remains a challenge due to the broad-spectrum UV–vis absorbance exhibited by many NPs, leading to a trade-off between transparency and heating efficiency.

Various approaches have been employed to develop semi-transparent photothermal coatings of noble metals on substrate surfaces. These methods include the deposition of randomly or sparsely assembled AuNPs and AgNPs,[26] the use of perforated Au films,[27] and the synthesis of Au-TiO_2 composites.[3,28,29] These coatings, depending on the plasmonic nanostructures, exhibit light absorption across a range of wavelengths from 420 nm to the infrared region. The resulting surfaces have found applications as solar radiator windows,[26] thermoplasmonic nanohole electrodes,[27] icephobic surface,[28] and antifogging coating.[3,29] Notably, Haechler et al. reported one of the best conditions for an antifogging coating, achieving an approximate temperature increase of 8.3 °C above ambient temperature (6.6 °C higher than the control), accompanied by a corresponding transmittance of 67.1%.[3]

In this paper, we developed a simple method for biotemplating metallic nanoparticles onto substrate surfaces. For this purpose, we used a flexible filamentous structure of potato virus A (PVA) VNPs, a less-explored material in the field of material science, as our template. The positively charged amino acid residues of PVA VNPs are effectively bound to negatively charged metallic nanoparticles (specifically, AgNPs coated with citric acid). Furthermore, we developed a novel technique that involved incorporating non-ionic surfactant micelles into a large, well-ordered protein matrix such as the PVA VNP liquid crystal (LC) phase. This enabled us to create spin-coated surface patterns with tunable vacant spaces. We have also developed a technique for chemically crosslinking these patterns to substrate surfaces, offering versatility for various downstream applications. Finally, the patterns were coated with AgNPs and evaluated for their photothermal effect and defogging efficiency. The presence of dense plasmonic hotspots along the PVA networks, separated by intermittent vacant spaces, resulted in a remarkable temperature increase of 21 °C above ambient temperature under 1-sun radiation. Moreover, these coated samples exhibited excellent transmittance of visible light (78%) at a wavelength of 550 nm. The coated samples also demonstrated significantly faster defogging compared to the uncoated samples, both in indoor and outdoor conditions.

2. Results and Discussion

2.1. Electrostatic Interaction Between PVA and Metallic NPs

The PVA capsid consists of ≈2000 proteinaceous subunits and carries either a positive or negative charge depending on its isoelectric point (pI) and solution pH.[30] At the pH equivalent to pI, the PVA particles are electrically neutral, while below and above the pI, they exhibit positive and negative charges, respectively. In our previous study on the structure and self-assembly behavior of PVA, we reported the charge distribution of a predicted model of PVA CP at pH 6, pH 7, and pH 8 using computer modeling.[31] However, in this work, we analyzed the charge distribution of a closely related virus-like particle from PVY using Poisson–Boltzmann server.[32] Figure S1 (Supporting Information) illustrates the surface charge distribution of PVY VNPs at different pHs. It is evident that at pH 7, the particles are mostly neutral, while the charges become increasingly positive/negative with decreasing/increasing pH, respectively. This gives a valuable means of manipulating the net charges of PVA particles by simply selecting a suitable buffer pH. For this reason, we chose this material platform as a candidate for biotemplating with oppositely charged substances via electrostatic interaction. In the current study, metallic nanoparticles, namely citrate-coated AuNPs and AgNPs, which are expected to possess a negative charge,[33] were chosen to decorate the PVA VNPs via electrostatic interactions (**Figure 1A**). The PVA VNPs were immobilized onto TEM grids and then incubated in a solution containing the metallic NPs. SEM images of filamentous PVA particles binding with AuNPs and AgNPs are shown in Figure 1B. From the figures, it is evident that the AuNPs and AgNPs are uniformly distributed on the surface of PVA with high selectivity, as there is minimal presence of Au or Ag on the substrates, which is confirmed by TEM and EDS signals (Figure 1C; Figure S2A,B, Supporting Information).

2.2. Controlling the PVA Film Morphology

To expand the application range of PVA – metallic NPs, it is essential to develop a reliable method for effectively depositing metallic NPs onto substrate surfaces using film deposition techniques. For that reason, spin-coating was chosen as a facile method for depositing PVA particles onto substrate surfaces. **Figure 2A** depicts the process of PVA deposition onto the substrate surface.

Interestingly, when the non-ionic surfactant Triton X-100 (TX-100) (Figure S3A, Supporting Information) was added to the PVA solution, pore-like textures were formed among the LC domains of PVA, as captured by polarized microscopy (Figure S3B, Supporting Information). TX-100 is known to form spherical micelles in aqueous solution,[34] thus those observed features resulted likely from the presence of TX-100 micelles. Similar to our previous study on PVA self-assembly using the drop-casting

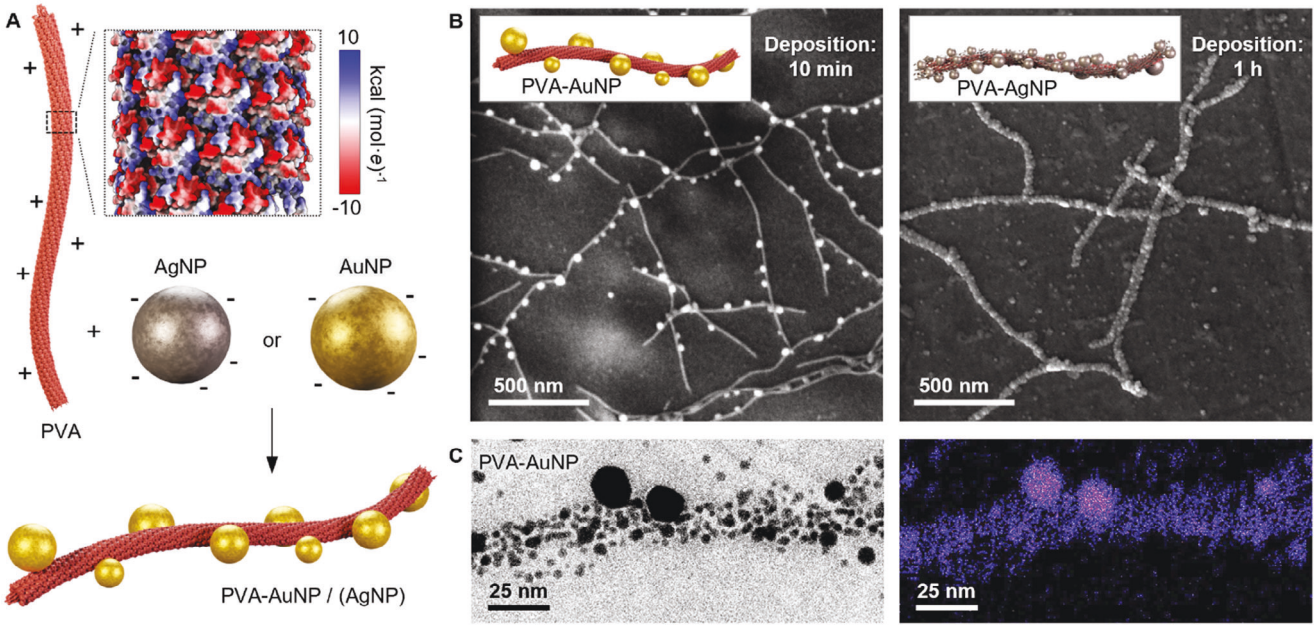

Figure 1. A) Schematic illustration depicting the surface charges of PVA VNPs and metallic NPs, as well as their electrostatic interaction. B) SEM images showing the binding of citric acid-coated AuNPs and AgNPs to PVA VNPs. C) STEM bright field image (left) and EDS image (right) verifying the specific attachment of AuNPs to PVA VNPs. In the EDS image, the purple color represents the location of Au.

technique,[31] the SEM image of the spin-coated PVA solution of concentration 3 mg mL^{-1}, showed a smooth film texture due to the parallel arrangement of PVA particles (Figure 2A). Figure S4 (Supporting Information) shows a collection of SEM images from the different areas across the substrate surface to validate the same. On the other hand, when the TX-100 was added to the PVA solution of the same concentration, we anticipated that the micelle structure would introduce microstructures in the spin-coated PVA film (Figure 2B). The SEM image of the film from TX-100 containing PVA solution indicated intermittent vacant spaces corresponding to the TX-100 micelles dispersed within the PVA matrix. This unique network could also be obtained by using Tween-20, demonstrating the general role of non-ionic surfactants in producing such patterns (Figure S5, Supporting Information).

2.3. Controlling the Surface Features of Spin-Coated PVA VNPs with Combination of Additives

To understand the impact of PVA, TX-100, and glycerol concentrations on the formation of PVA VNP nanopatterns, we

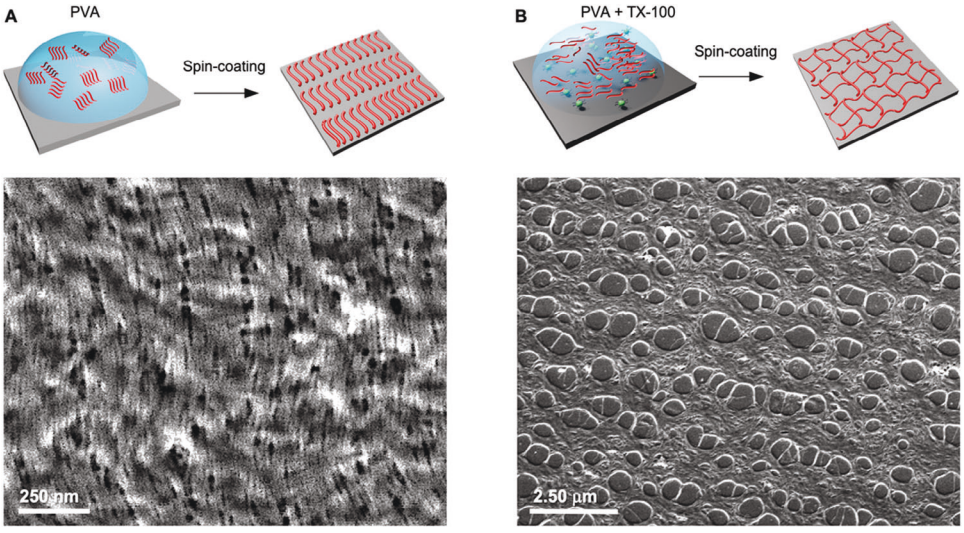

Figure 2. Schematic illustration of the spin-coating process, and SEM images below displaying the resulting patterns on silicon substrates for two different solutions: A) PVA and B) PVA combined with TX-100.

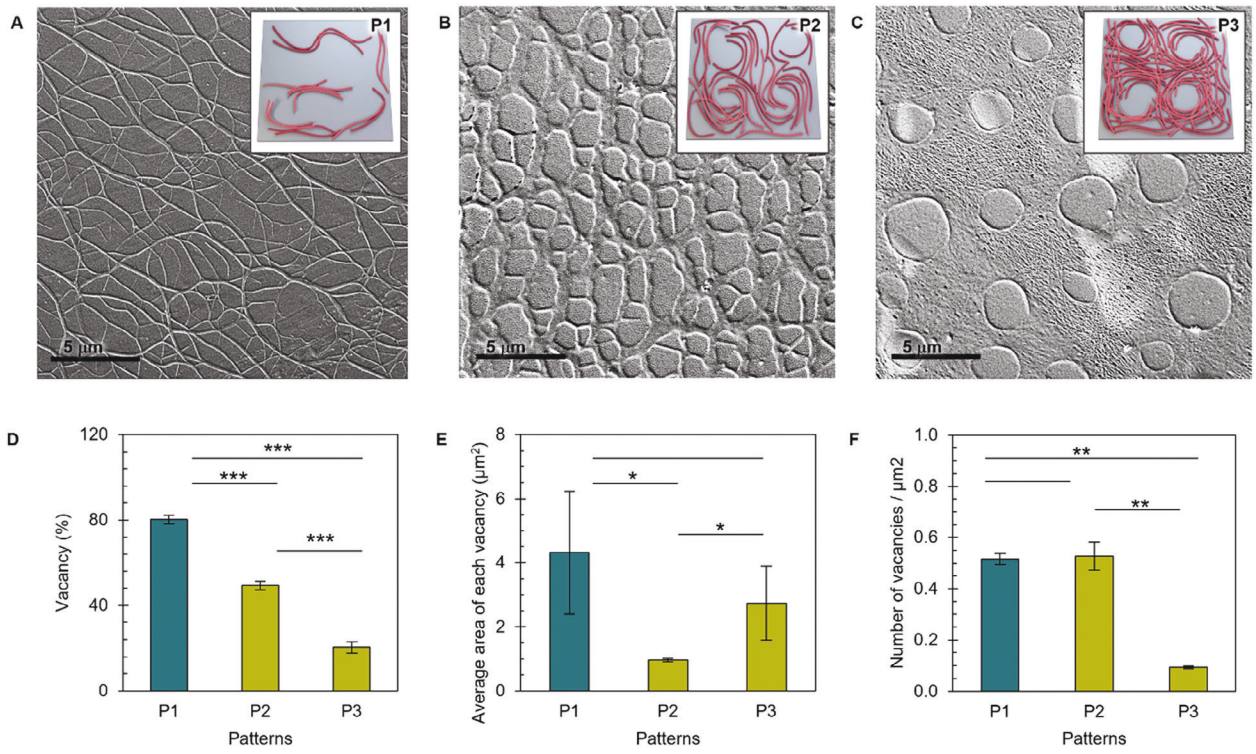

Figure 3. A–C) SEM images of patterns generated from three distinct solutions: P1 (PVA 1 mg mL^{-1}, TX-100 1%, Glycerol 2%), P2 (PVA 2 mg mL^{-1}, TX-100 1%, Glycerol 2%), and P3 (PVA 2 mg mL^{-1}, TX-100 1%, Glycerol 6%), all on silicon substrates. Inset images provide a schematic representation of the network structure for each respective pattern. D–F) Graphs depicting the following parameters for each pattern type: the total percentage of vacant area ($n = 4$), the average area of individual vacant spots ($n = 4$), and the number of vacant spots per unit area ($n = 3$). Error bars represent standard deviation. Asterisks indicate statistically significant differences between adjacent values. Specifically, *, **, and *** correspond to $p < 0.05$, $p < 0.01$, and $p < 0.001$, respectively.

systematically varied these factors and analyzed their effects on the morphology of spin-coated PVA films. The film morphologies were characterized based on several parameters, including the percentage of total vacant areas in relation to the entire film, the average area of each vacancy, and the number of vacancies per unit area (Figure S6A–I, Supporting Information). The concentration ranges for PVA, TX-100, and glycerol were 1–4 mg mL^{-1}, 0.5–3%, and 2–6%, respectively. The effects of PVA on the film properties were straightforward to follow. As the concentration of PVA VNPs increased, the vacancy percentage, average area of each vacancy, and number of vacancies per unit area, all showed a decreasing trend (Figure S6A–C, Supporting Information). Conversely, the effects of TX-100 and glycerol exhibited an opposite trend in terms of vacancy coverage and number of vacancies per unit area (Figure S6D,F,G,I, Supporting Information). However, the average area of vacancy did not show a clear trend in either case (Figure S6E,H, Supporting Information). The reason behind the contrasting behavior between TX-100 and glycerol is not entirely clear, although it is possible that glycerol could influence micelle number and properties, as well as the surface tension of the liquid phase. Additionally, the non-monodispersed nature of the micelles may contribute to the high standard deviation in the average area of vacancies and the lack of a discernible trend.

In this manuscript, we selected three distinct patterns, namely P1, P2, and P3, which differ from each other both visually (**Figure** 3A–C) and in terms of their properties (Figure 3D–F). The experimental conditions of each pattern were as follows: P1 (PVA 1 mg mL^{-1}, TX-100 1%, Glycerol 2%), P2 (PVA 2 mg mL^{-1}, TX-100 1%, Glycerol 2%), and P3 (PVA 2 mg mL^{-1}, TX-100 1%, Glycerol 6%). P1 appeared to be a wire-like network that predominantly contained vacancies, with irregular shapes (Figure 3A). In P2 and P3, the coverage of vacancies was significantly lower, and the vacancies exhibited more regular shapes (Figure 3B,C). Interestingly, when we applied the same experimental conditions to an unrelated monomeric protein, bovine serum albumin (BSA), we were unable to obtain similar patterns (Figure S7, Supporting Information). Unlike the organized filamentous polymer-like structure of PVA, the patterns produced by BSA appeared as smooth films with rounded holes resulting from TX-100 micelles. This highlights the importance of utilizing macromolecular assemblies like PVA to achieve diverse and tunable surface patterns.

2.4. Stabilization of PVA Patterns on Substrate Surfaces and Preliminary Photothermal Testing

The next phase of our work involved using P1, P2, and P3 as templates to decorate substrate surfaces with networks of AgNPs. However, as we further exposed the patterns to an aqueous environment, they disappeared (Figure S8A–F, Supporting Information). As can be seen in Figure S8D–F (Supporting

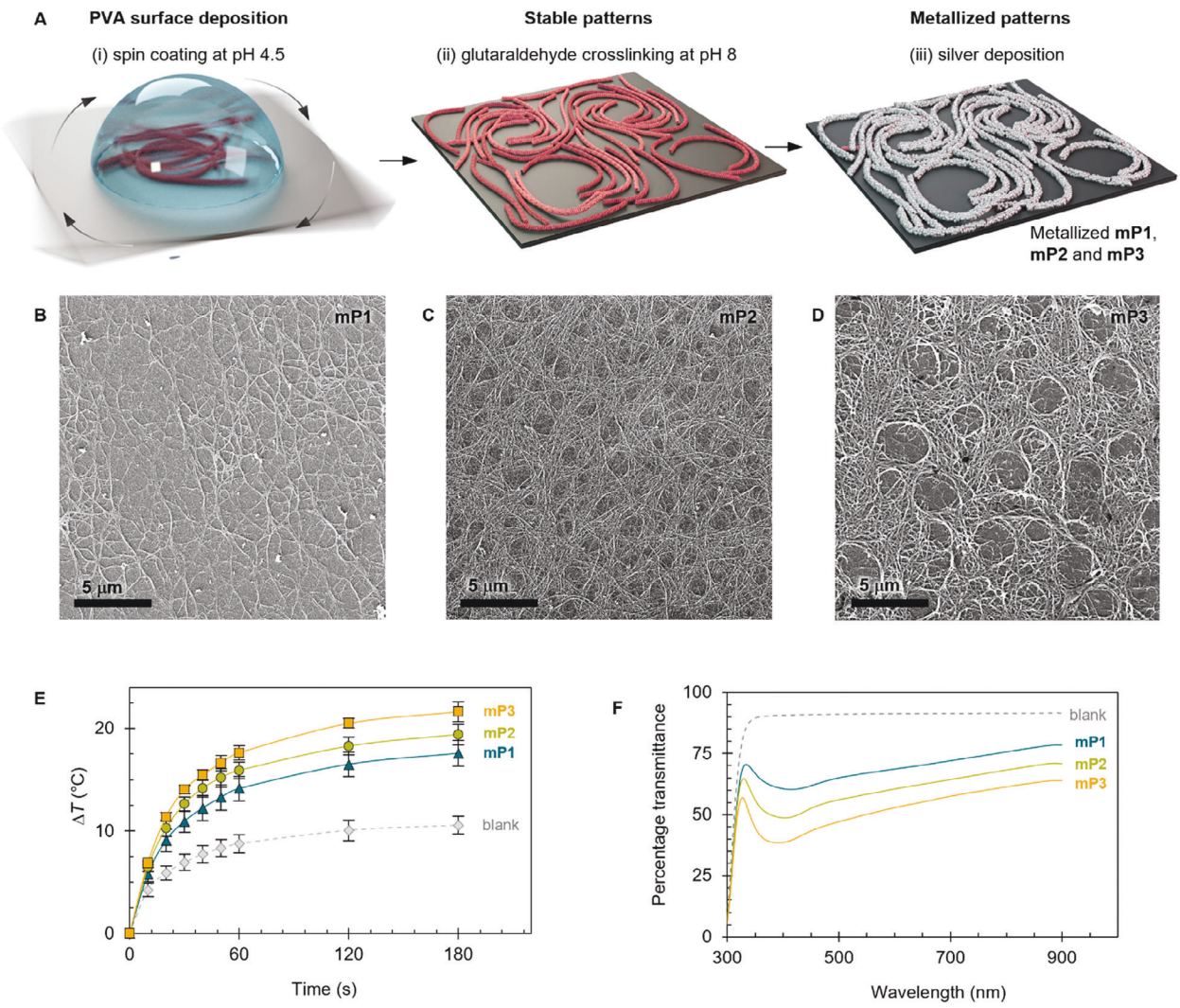

Figure 4. A) Schematic illustration demonstrating the process of creating bio-templated metalized patterns on a glass substrate. B–D) SEM images showing metalized patterns mP1, mP2, and mP3 after AgNP binding, respectively. E) Time-resolved profiles showing the increase above ambient temperature (23 °C) for both the unpatterned (blank) and patterned samples exposed to 1-sun radiation. $n = 4$ and error bars represent the standard deviation. F) UV–vis transmittance measurements for the blank and patterned samples.

Information), the deposition of AgNPs resulted in patterns P1, P2, and P3 losing their original morphology. The transient nature of the patterns could be attributed to the absence of physical or chemical interactions between the VNPs and the substrate. To address this issue, we decided to crosslink the patterns to the substrate surfaces. Since our chosen substrate primarily consisted of silica-based materials such as glass or silicon wafers, we first treated the surfaces with APTES to introduce a positive charge. Next, we spin-coated the PVA solutions onto the APTES-coated surfaces at pH 4.5, using the same conditions as P1, P2, and P3. The rationale behind this approach was that both PVA at pH 4.5 and APTES would carry positive charges, allowing the PVA particles to spread freely without hindrances from attractive forces stemming from opposite charges, such as those observed with PVA VNPs above pH 7 (Figure S1, Supporting Information). We then incubated the substrates with the patterns at pH 8, using a 0.1 M HEPES buffer, causing the particles to acquire a negative charge and bind to the APTES-coated surfaces via electrostatic interaction. To further stabilize the patterns, PVA VNPs were anchored to the NH_2 groups of APTES-coated surfaces with 10% glutaraldehyde. After this treatment, AgNPs were deposited onto the templates (**Figure** 4A). The crosslinking approach successfully preserved much of the original patterns even after AgNPs deposition (Figure 4B–D). However, it is worth noting that stabilizing the P3 patterns proved to be more challenging compared to the other two patterns. Therefore, an additional step was incorporated, involving the immobilization of α-CP onto the APTES-coated surface before the spin coating of PVA VNPs.

Finally, we tested the photothermal effect and transmittances of the stabilized patterns (Figure 4E,F). Interestingly, the achieved temperatures were strongly influenced by the surface patterns made by PVA VNPs. Moreover, the temperature attained by each pattern exhibited an inverse relationship with the corresponding transmittances. The key factor that correlated with

transmittances was the percentage of vacant areas within the patterns (Figure S9, Supporting Information). Also, all transmission spectra displayed a significant decrease in transmittance near the wavelength of 400 nm, indicating the predominance of spherical-shaped AgNPs with absorption maxima in that region.[35] Furthermore, the decreasing transmittance near 400 nm for metalized patterns mP1, mP2, and mP3 indicated an increasing amount of AgNPs bound to the surface, which could be attributed to the enhanced coverage of PVA on the surface (inverse of vacancy percentage as reported in Figure 3D). Interestingly, APTES treatment of the surfaces introduced free amino groups capable of binding negatively charged AgNPs. However, in comparison to mP2, the achieved temperature was significantly lower, suggesting the positive effects of dense plasmonic hotspots along the PVA scaffolds on the photothermal effect produced by mP2 (Figure S10, Supporting Information). Following overnight deposition of AgNPs onto the PVA patterns, the highest temperature increase above the ambient temperature after 3 min of exposure under 1-sun intensity light was 21.63°C (11.07°C above the blank) for mP3. The corresponding transmittance of the visible light measured at 550 nm was ≈45%. In comparison to the state-of-the-art transparent photothermal material reported by Haechler et al.,[3] the temperature profile we obtained was better, but the transmittance was relatively low. In the case of mP2, we achieved a temperature increase of 19.43 °C above the ambient temperature (8.83 °C above the blank) with a reasonable transmittance of 55%. Due to the additional challenges in stabilizing the P3 patterns, we proceeded with mP2 for the subsequent studies.

2.5. Controlling Photothermal Effect of PVA-AgNP Patterned Surface

Based on the previous experiment, we observed a proportional relationship between the temperature attained by the PVA-AgNPs material and the reduction in transmittance near the 400 nm wavelength range (Figure 4E,F), which, in turn, corresponded to the degree of PVA coverage, and thus the amount of AgNPs deposited on the surface (Figure S9, Supporting Information). Therefore, in this study, we investigated the role of incubation pH, incubation time, and Ag-seed concentration on AgNP deposition on the mP2 template. We measured the combined thicknesses of the PVA-AgNPs hybrid material, and the maximum temperature attained after 3 min of exposure to 1-sun radiation for all studied parameters (**Figure 5**A–C). Their corresponding thickness profiles measured with a stylus profilometer, can be found in Figure S11A–I (Supporting Information), and the absorbances at 420 nm in Figure S11J–L (Supporting Information). Based on the thickness results (Figure 5A), AgNP deposition increased as the pH decreased during incubation (Figure S11A,D,G,J, Supporting Information). This can be easily understood since the PVA VNPs, similar to PVY VLPs (Figure S1, Supporting Information), are expected to be more positively charged at lower pH, leading to a higher capture of AgNPs compared to those at higher pH. On the other hand, an increase in incubation time and AgNP seed concentration led to enhanced AgNP deposition, as indicated by the thickness results (Figure 5B,C). Interestingly, the thickness results aligned well with the combined diameters of PVA VNPs and AgNPs which are ≈11–14[36] and 10–20 nm, respectively (Figure S11M, Supporting Information), showing that the surface patterns are produced by PVA VNPs coated with dense arrays of AgNPs. the profiles of AgNP deposition consistently correlated with the absorption values at 420 nm, corresponding to UV–vis absorption peak for AgNPs (Figure S11J–L, Supporting Information). Also, the maximum temperatures attained showed a positive correlation with the extent of AgNP deposition (Figure 5A–C; Figure S11J–L, Supporting Information).

Based on the aforementioned experiments, we selected the following combination for testing photothermal activity and UV–vis transmittance: pH 4.5, incubation time of 60 min, and AgNPs concentration of 1.5X. The highest temperature obtained after 3 min of light exposure was 21 °C above the ambient temperature (7.6 °C above the blank) (Figure 5D). Notably, the corresponding transmittance of visible light measured at 550 nm reached ≈78% (Figure 5E). This notable combination of high temperature and high transmittance can be attributed to the presence of dense plasmonic hotspots produced by well-organized AgNPs (<20 nm) and the intricate interconnected network of PVA VNPs (Figure S11M, Supporting Information) intermittently separated by vacant areas, allowing for highly efficient light transmission.

2.6. Defogging Performance of PVA-AgNPs Pattered Surface

In the final stage of our study, we assessed the defogging efficiency of the PVA-AgNPs patterned mP2 described in Figure 5D,E. Defogging experiments were conducted under both indoor and outdoor conditions. In the indoor experiment, we placed the coated substrate and an uncoated reference substrate on top of a Peltier element to maintain a constant temperature of 23 °C. Both surfaces were directly exposed to 1-sun intensity light from a sun simulator for 2 min (**Figure 6**A). Then we saturated both surfaces with vapor droplets generated by a commercial steam generator and allowed them to naturally defog. The entire defogging process was recorded using a camera (Video S2, Supporting Information), and a time-resolved defogging profile was extracted for both the coated and the blank samples through image analysis (Figure 6B,C). The results clearly demonstrate that the coated samples exhibit significantly faster defogging compared to the reference samples. In most cases, by the time the coated samples were completely defogged, ≈80% of the control samples remained covered with fog. Comparative analysis of the total defogging time at different set temperatures revealed that the coated samples defogged 2–3 times faster than the reference samples (Figure S12A,C, Supporting Information), achieving a performance comparable to the current standard.[3] Furthermore, we evaluated the real-life performance of the PVA-AgNPs hybrid coating outdoors under natural sunlight, equivalent to 0.5 sun intensity (Figure 6D) and temperature 16 °C. Remarkably, even with a lower sun intensity, the coated sample defogged at least two times faster than the control samples (Figure S12B,C and Video S3, Supporting Information)

3. Conclusion

In summary, we have developed a spin-coating-based method to pattern substrate surfaces on a large scale using PVA VNPs.

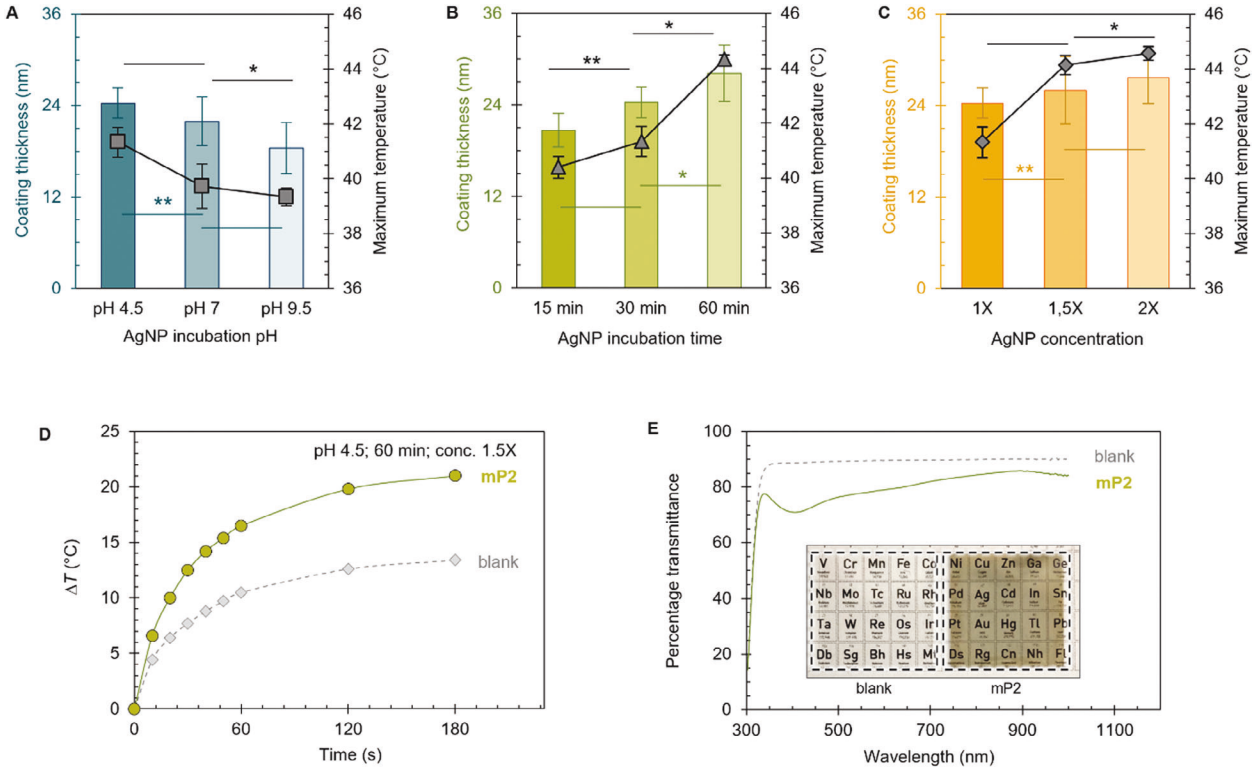

Figure 5. A–C) Graphs showing the influence of various factors on the thickness of PVA–AgNP hybrid networks (bar graph, primary axis) and their associated photothermal performance (line graph, secondary axis). A) PVA-AgNPs were incubated for 30 min in 1X AgNP solution at pH 4.5, pH 7, and pH 9.5. B) PVA-AgNPs were incubated for 15, 30, and 60 min in 1X AgNP solution at pH 4.5. C) PVA-AgNPs were incubated for 30 min in 1X, 1.5X, and 2X AgNP solution at pH 4.5. For all the temperature datasets $n = 3$. For all the thickness datasets $n = 4$ (except for 2X $n = 3$). Error bars represent standard deviation. Statistically significant differences between adjacent data points on the bar graphs are indicated by asterisks positioned above, whereas the line graphs display such differences below them. Specifically, * and ** correspond to $p < 0.05$ and $p < 0.01$, respectively. D) Time-resolved profiles showing the increase above ambient temperature (23 °C) for unpatterned (blank) and mP2 samples exposed to 1-sun radiation. E) UV–vis transmittance measurements for the blank and mP2 samples. Inset shows the photographs of the blank and mP2 patterns against texts to demonstrate the transparency of the coated surface.

These patterns consist of interconnected PVA networks with adjustable vacant spaces created by TX-100 micelles. The remarkable flexibility of the VNPs, combined with their strong affinity for the outer layer of surfactant micelles containing hydrophilic headgroups, has led to the formation of intricate patterns that can be tailored by adjusting the concentrations of VNPs and surfactant. Additionally, we have established a controlled coating to deposit AgNPs onto the VNP patterns. The presence of numerous plasmonic hotspots, interspersed with vacant areas, has facilitated the realization of exceptional photothermal behavior while maintaining excellent light transmittance properties. Finally, our coated samples have exhibited highly efficient defogging capabilities in both indoor and outdoor conditions. These findings highlight the versatility and practicality of our approach, making it a promising avenue for various photothermal applications.

4. Experimental Section

Production and Purification of PVA VNPs: PVA VNPs were produced and isolated from their host plants *Nicotiana benthamiana*. The plants were grown at 22 °C under 16 h (light) and 8 h (dark) photoperiod in environmentally controlled greenhouses. Young plants at the 4-leaves stage were infected with *Agrobacterium* carrying PVA infectious complementary DNA (icDNA). Leaves from systemically infected plants were harvested after three weeks of agroinfiltration and stored at −80 °C. PVA VNPs were purified following the protocol described in Ref.[31]

In Silico Analysis of Charge Distribution of Potato Virus Y (PVY) Virus-Like Particles (VLP) at Different pH Levels: The cryo-EM structure of PVY VLP (PDB ID: 6HXZ), which is a related virus belonging to the same genus potyvirus, was analyzed for the calculation of electrostatics at different pHs. The charge distribution model of PVY VLPs was generated using the APBS-PDB2PQR software hosted by a server (https://server.poissonboltzmann.org/). The model was visualized using the software ChimeraX 1.2.5.

Spin-Coating of PVA VNPs: PVA VNPs were deposited on the substrates via spin-coating (Laurell Technologies WS-650Mz-23NPPB). For this, the substrates were first securely mounted on the spin coating stage using a vacuum pump. Then the substrate surfaces were covered with a PVA solution of appropriate pH (0.1 M ammonium acetate buffer) and concentration (with or without additives). Finally, the spin coating process was carried out at 3000 rpm for 1 min.

Silanization of Glass Surface: Glass substrates were subjected to a cleaning process, initially by sonicating them in ethanol for 10 min, followed by rinsing them in MilliQ water twice for 10 min each. The cleaned glass surfaces were then activated using oxygen plasma treatment at 100 W for 3 min using Henniker Plasma HPT-100. The activated glass surfaces were then immersed in a solution of 5% (3-Aminopropyl)triethoxysilane (APTES) in ethanol for 16 h. Afterward,

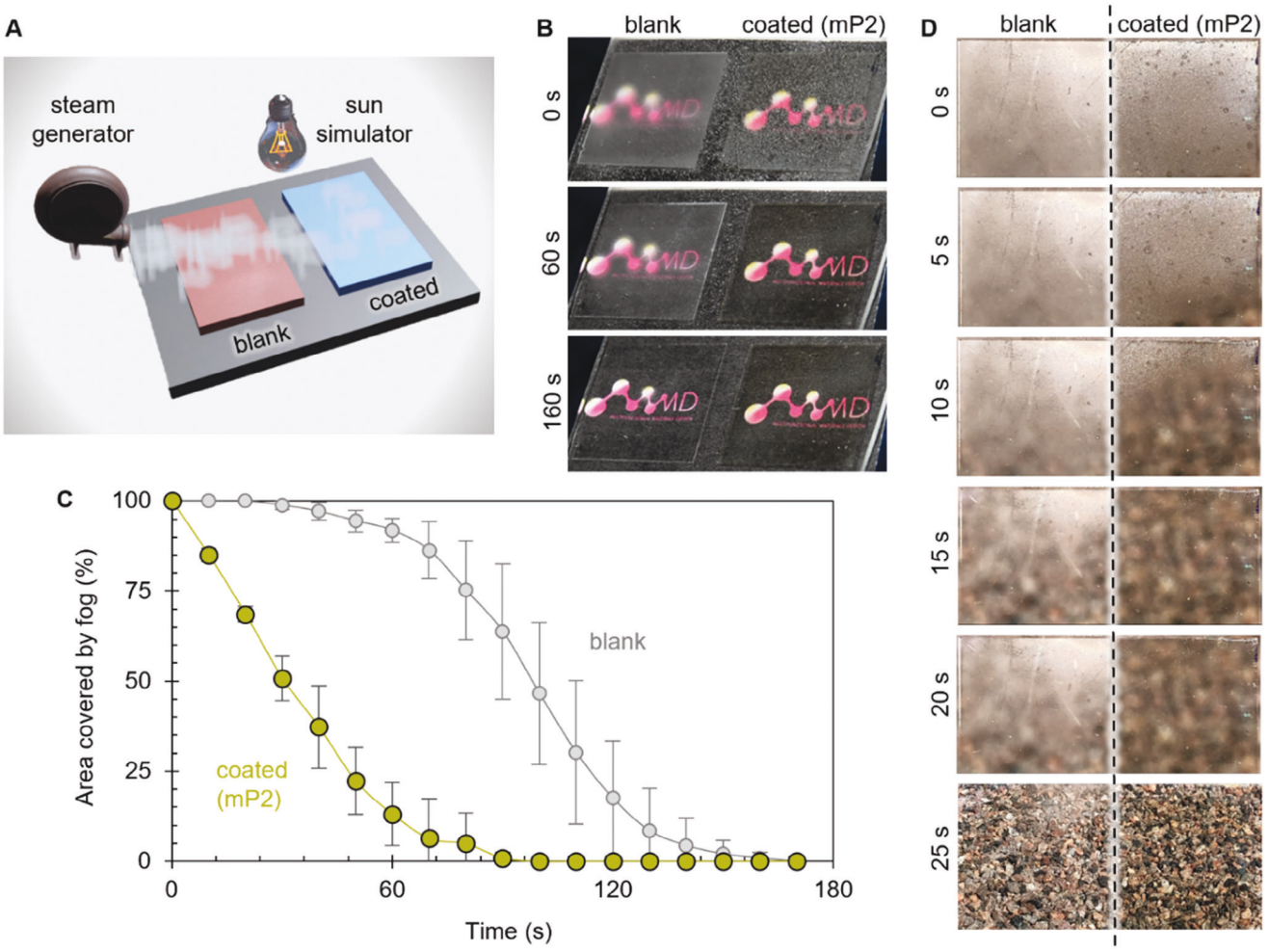

Figure 6. A) Schematic illustration demonstrating the defogging experiment. B) A series of time-sequence photographs illustrating the defogging process of the uncoated (blank) and coated samples under indoor conditions. C) Time-resolved profiles presenting the percentage of the area covered by fog for the blank and coated samples when exposed to 1-sun radiation. $n = 3$ and error bars represent the standard deviation. D) A series of time-sequence photographs illustrating the defogging process of the blank and coated samples under outdoor conditions, where the intensity of actual sunlight was equivalent to 0.5-sun.

APTES-treated glass substrates underwent sonication in ethanol for 20 min, followed by two additional rounds of sonication in MilliQ water for 20 min each. The dried APTES-treated substrates were then used within 24 h.

Preparation of AgNP Seed Solution: The synthesis of silver nanoparticles (AgNPs) was conducted following a previously reported procedure.[37] In brief, citrate-capped AgNPs were synthesized by mixing 2.5×10^{-4} M $AgNO_3$ and 2.5×10^{-4} M trisodium citrate in 20 mL deionized water. Subsequently, 600 µL of ice-cold, freshly prepared 0.1 M $NaBH_4$ solution was swiftly introduced into the solution while vigorously stirring. The addition of $NaBH_4$ caused an immediate change in the solution's color to yellow, indicating the formation of NPs. These NPs were employed as seeds within a time frame of 2–5 h after the synthesis. The resulting concentration of AgNPs is referred to as "1X" in the rest of the manuscript.

Templating PVA VNPs with AgNPs: PVA VNPs were immobilized on substrate surfaces using a two-step process. First, the substrate surfaces were coated either with only APTES as described in "Silanization of Glass Surface", or APTES with an additional layer of an antibody against PVA coat protein (α-CP). The latter is achieved by simply incubating APTES-treated substrates with 1:1000 solution of α-CP at pH 8 for 30 min. α-CP molecules were supposed to bind the positively charged APTES side chains via electrostatic interaction. Subsequently, the particles were crosslinked to the surface by incubating the PVA patterned surface in a 10% glutaraldehyde at pH 8 (0.1 M HEPES buffer). This step served the dual purpose of facilitating the electrostatic or antibody-mediated binding of VNPs to the APTES or α-CP, as well as the crosslinking of the NH_2 side chains of the VNPs with the NH_2 groups of the APTES coated surface or α-CPs. Finally, the substrates were placed face down, with the patterned side immersed in an AgNP solution adjusted to the desired pH using 0.1 M ammonium acetate buffer. Simultaneous agitation was applied using a magnetic bead (Video S1, Supporting Information). After the required incubation period, the AgNP-templated surfaces were washed by incubating in 0.1 (M) ammonium acetate buffer at pH 4.5 for 30 min followed by MilliQ water for 30 min to remove any unbound AgNPs and then dried using nitrogen gun for subsequent analysis.

UV–Vis Transmittance and Absorbance Measurement: The transmittance and absorbance of the substrates were measured using a UV-2600 spectrophotometer (Shimadzu, Japan) across a wavelength range of 200–1000 nm.

Thickness Calculation with Stylus Profilometer: The film thickness was measured using a Veeco Dektak 6 M mechanical profilometer. To measure

the thickness, the substrates with thin films were intentionally scratched. A 12.5 µm stylus was used to scan a 5 mm section of the surface within 30 s, applying a force of 3 mg.

Processing of Data from Images: The characterization of vacancies in the PVA network was performed using the image processing software ImageJ developed by the National Institutes of Health. SEM images were imported into ImageJ, and adjustments were made to the contrast and color threshold settings to achieve accurate segmentation of PVA filaments and vacancies. Subsequently, the number of vacancies and the corresponding vacancy areas were automatically calculated using the particle analysis function within the software. Similarly, the area covered by fog in the samples was determined using the same method. In cases where SEM images or photographs had low contrast, image segmentation was manually performed using the area selection tool, followed by the particle analysis step to obtain the final results.

Visualization of the VNPs and AgNPs: PVA VNPs, AgNPs, and AuNPs were visualized using a Tescan Mira 3 scanning electron microscope (SEM) and a JEM-2800 transmission electron microscope (TEM). The presence of Ag and Au was further confirmed using energy dispersive spectrometry (EDS) coupled with the JEM-2800 TEM, which allowed for precise mapping of the element of interest.

Analysis of Photothermal Activity and Defogging Behaviour: Glass substrates (Corning 18 mm × 18 mm, Cat No. 2845-18) were exposed to 1-sun radiation using a sun simulator (11 002 SunLite, Abet Technologies). The temperature change was monitored using a thermocouple thermometer (UNI-T UT320 series) with a probe placed beneath the substrate surface. For the defogging experiment, the substrates were first brought to a stable temperature using a Peltier element. Next, the substrates were exposed to steam generated by a steam generator (Tefal–Access Steam Minute DT7000E0). The defogging process was recorded using a camera to capture the defogging profile.

Supporting Information

Supporting Information is available from the Wiley Online Library or from the author.

Acknowledgements

The research was funded by The Ella Georg Ehrnrooth Foundation, the European Research Council (H2020) StG "Autonomously adapting and communicating modular textiles" No. 949 648 and No. 101 002 258, ModelCom, Academy of Finland SUPER-WEAR project (decision number: 322 214), Academy of Finland's Flagship Programme under Project Nos. 318 890 and 318 891 (Competence Center for Materials Bioeconomy, FinnCERES) and Centers of Excellence Programme (2022–2029) in Life-Inspired Hybrid Materials (LIBER), project number 346 110. Research in the Mäkinen lab (University of Helsinki) is supported by the Academy of Finland (decision 332 950). Further, the authors acknowledge OtaNano Nanomicroscopy Center at Aalto University for their facilities and expertise that were crucial for the stylus profilometer and TEM studies carried out in this work. The authors also acknowledge the HiLIFE Biocomplex unit at the University of Helsinki, a member of Instruct-ERIC Centre Finland, FINStruct, and Biocenter Finland for their facilities and expertise that were crucial for the purification of PVA VNPs.

Conflict of Interest

The authors declare no conflict of interest.

Author Contributions

S.D. performed funding acquisition, conceptualization, methodology, and writing. H.M.N. performed analysis, methodology, and writing. F.Z. performed analysis, methodology, review, and editing. F.B. performed analysis, methodology, review, and editing. M.M. performed analysis, methodology, review, and editing. K.M. performed supervision, project administration, review, and editing. M.K. performed funding acquisition, supervision, review, and editing. J.V. performed funding acquisition, supervision, project administration, review, and editing.

Data Availability Statement

The data that support the findings of this study are available from the corresponding author upon reasonable request.

Keywords

antifogging coating, biohybrid functional material, photothermal metamaterial, plant virus nanotechnology, silver nanoparticles

Received: October 3, 2023
Revised: November 27, 2023
Published online: December 19, 2023

[1] W. J. Stark, P. R. Stoessel, W. Wohlleben, A. Hafner, *Chem. Soc. Rev.* **2015**, *44*, 5793.
[2] P. Wang, A. V. Krasavin, L. Liu, Y. Jiang, Z. Li, X. Guo, L. Tong, A. V. Zayats, *Chem. Rev.* **2022**, *122*, 15031.
[3] I. Haechler, N. Ferru, G. Schnoering, E. Mitridis, T. M. Schutzius, D. Poulikakos, *Nat. Nanotechnol.* **2023**, *18*, 137.
[4] A. Korpi, E. Anaya-Plaza, S. Välimäki, M. Kostiainen, *Wiley Interdiscip. Rev. Nanomed. Nanobiotechnol.* **2020**, *12*, e1578.
[5] M. A. Kostiainen, P. Hiekkataipale, A. Laiho, V. Lemieux, J. Seitsonen, J. Ruokolainen, P. Ceci, *Nat. Nanotechnol.* **2013**, *8*, 52.
[6] L. A. Lee, Z. Niu, Q. Wang, *Nano Res.* **2009**, *2*, 349.
[7] J. K. Pokorski, N. F. Steinmetz, *Mol. Pharmaceutics* **2011**, *8*, 29.
[8] T. L. Schlick, Z. Ding, E. W. Kovacs, M. B. Francis, *J. Am. Chem. Soc.* **2005**, *127*, 3718.
[9] M. A. Bruckman, G. Kaur, L. A. Lee, F. Xie, J. Sepulveda, R. Breitenkamp, X. Zhang, M. Joralemon, T. P. Russell, T. Emrick, Q. Wang, *ChemBioChem* **2008**, *9*, 519.
[10] N. F. Steinmetz, M. E. Mertens, R. E. Taurog, J. E. Johnson, U. Commandeur, R. Fischer, M. Manchester, *Nano Lett.* **2010**, *10*, 305.
[11] A. A. A. Aljabali, J. E. Barclay, G. P. Lomonossoff, D. J. Evans, *Nanoscale* **2010**, *2*, 2596.
[12] V. Liljeström, A. Ora, J. Hassinen, H. T. Rekola, Nonappa, M. Heilala, V. Hynninen, J. J. Joensuu, R. H. A. Ras, P. Törmä, O. Ikkala, M. A. Kostiainen, *Nat. Commun.* **2017**, *8*, 671.
[13] A. Chakraborty, Nonappa, B. Mondal, K. Chaudhari, H. Rekola, V. Hynninen, M. A. Kostiainen, R. H. A. Ras, T. Pradeep, *J. Phys. Chem. C* **2021**, *125*, 3256.
[14] L. Wang, X. Xu, Q. Cheng, S. X. Dou, Y. Du, *Small* **2021**, *17*, 1904107.
[15] J. Chen, Z. Ye, F. Yang, Y. Yin, *Small Sci.* **2021**, *1*, 2000055.
[16] C. Kuppe, K. R. Rusimova, L. Ohnoutek, D. Slavov, V. K. Valev, *Adv. Opt. Mater.* **2020**, *8*, 1901166.
[17] C. Liu, J. Huang, C.-E. Hsiung, Y. Tian, J. Wang, Y. Han, A. Fratalocchi, *Adv. Sustain. Syst.* **2017**, *1*, 1600013.
[18] W. Li, C. Lin, W. Ma, Y. Li, F. Chu, B. Huang, S. Yao, *Cell Rep. Phys. Sci.* **2021**, *2*, 100435.
[19] S. Anuthum, F. Hasegawa, C. Lertvachirapaiboon, K. Shinbo, K. Kato, K. Ounnunkad, A. Baba, *Phys. Chem. Chem. Phys.* **2022**, *24*, 7060.
[20] D. Kim, R. Amatya, S. Hwang, S. Lee, K. A. Min, M. C. Shin, *Pharmaceutics* **2021**, *13*, 575.

[21] J. Zhang, J. Wang, G. Fan, B. Zhang, G. Ma, H. Xiao, L. Wang, *Polymers* **2022**, *14*, 2787.
[22] V. O. Shipunova, M. M. Belova, P. A. Kotelnikova, O. N. Shilova, A. B. Mirkasymov, N. V. Danilova, E. N. Komedchikova, R. Popovtzer, S. M. Deyev, M. P. Nikitin, *Pharmaceutics* **2022**, *14*, 1013.
[23] L. A. Austin, M. A. Mackey, E. C. Dreaden, M. A. El-Sayed, *Arch. Toxicol.* **2014**, *88*, 1391.
[24] M. Kim, J.-H. Lee, J.-M. Nam, *Adv. Sci.* **2019**, *6*, 1900471.
[25] I.-W. Un, Y. Sivan, *J. Appl. Phys.* **2019**, *126*, 173103.
[26] M. Guo, L. Gao, Y. Wei, Y. Ma, Y. Jianyong, B. Ding, *Sol. Energy Mater. Sol. Cells* **2021**, *219*, 110796.
[27] D. Tordera, D. Zhao, A. V. Volkov, X. Crispin, M. P. Jonsson, *Nano Lett.* **2017**, *17*, 3145.
[28] E. Mitridis, T. M. Schutzius, A. Sicher, C. U. Hail, H. Eghlidi, D. Poulikakos, *ACS Nano* **2018**, *12*, 7009.
[29] C. Walker, E. Mitridis, T. Kreiner, H. Eghlidi, T. M. Schutzius, D. Poulikakos, *Nano Lett.* **2019**, *19*, 1595.
[30] B. Michen, T. Graule, *J. Appl. Microbiol.* **2010**, *109*, 388.
[31] S. De, H. M. Nguyen, V. Liljeström, K. Mäkinen, M. A. Kostiainen, J. Vapaavuori, *Virology* **2023**, *578*, 103.
[32] E. Jurrus, D. Engel, K. Star, K. Monson, J. Brandi, L. E. Felberg, D. H. Brookes, L. Wilson, J. Chen, K. Liles, M. Chun, P. Li, D. W. Gohara, T. Dolinsky, R. Konecny, D. R. Koes, J. E. Nielsen, T. Head-Gordon, W. Geng, R. Krasny, G.-W. Wei, M. J. Holst, J. A. Mccammon, N. A. Baker, *Protein Sci.* **2018**, *27*, 112.
[33] N. M. Cativa, I. E. Dell'erba, C. V. Waiman, G. F. Arenas, M. Ceolín, L. J. Giovanetti, J. M. Ramallo-López, G. Eliçabe, C. E. Hoppe, *Langmuir* **2020**, *36*, 13998.
[34] L. Zhang, X. Chai, P. Sun, B. Yuan, B. Jiang, X. Zhang, M. Liu, *Molecules* **2019**, *24*, 1649.
[35] B. J. Wiley, S. H. Im, Z.-Y. Li, J. Mclellan, A. Siekkinen, Y. Xia, *J. Phys. Chem. B* **2006**, *110*, 15666.
[36] E. V. Shtykova, M. V. Petoukhov, N. V. Fedorova, A. M. Arutyunyan, E. V. Skurat, L. V. Kordyukova, A. V. Moiseenko, A. L. Ksenofontov, *Biochem* **2021**, *86*, 230.
[37] F. Basarir, T.-H. Yoon, *Ultrason. Sonochem.* **2012**, *19*, 621.